DEVELOPMENT OF ATOMIC FORCE MICROSCOPY SYSTEM AND KELVIN
PROBE MICROSCOPY SYSTEM FOR USE IN SEMICONDUCTOR
NANOCRYSTAL CHARACTERIZATION

A THESIS SUBMITTED TO
THE GRADUATE SCHOOL OF NATURAL AND APPLIED SCIENCES
OF
MIDDLE EAST TECHNICAL UNIVERSITY

BY

UMUT BOSTANCI

IN PARTIAL FULFILLMENT OF THE REQUIREMENTS
FOR
THE DEGREE OF MASTER OF SCIENCE
IN
PHYSICS

AUGUST 2007

Approval of Thesis

DEVELOPMENT OF ATOMIC FORCE MICROSCOPY SYSTEM AND KELVIN PROBE MICROSCOPY SYSTEM FOR USE IN SEMICONDUCTOR NANOCRYSTAL CHARACTERIZATION

Submitted by **Umut BOSTANCI** in partial fulfillment of the requirements for the degree of **Master of Science in Physics Department, Middle East Technical University** by,

Prof. Dr. Canan ÖZGEN
Dean, Graduate School of **Natural and Applied Sciences** _____

Prof. Dr. Sinan BİLİKMEN
Head of Department, **Physics** _____

Prof. Dr. Raşit TURAN _____
Supervisor, **Physics Dept., METU**

Examining Committee Members:

Prof. Dr. Çiğdem ERÇELEBİ
Physics Dept., METU _____

Prof. Dr. Raşit TURAN
Physics Dept., METU _____

Prof. Dr. Mehmet PARLAK
Physics Dept., METU _____

Assoc. Prof. Dr. Necati Özkan
Central Laboratory, METU _____

Dr. Aykutlu DÂNA _____
Physics Dept., Bilkent University

Date: _____

I hereby declare that all information in this document has been obtained and presented in accordance with academic rules and ethical conduct. I also declare that, as required by these rules and conduct, I have fully cited and referenced all material and results that are not original to this work.

Name SURNAME : Umut BOSTANCI
Signature   :

ABSTRACT

DEVELOPMENT OF ATOMIC FORCE MICROSCOPY SYSTEM
AND KELVIN PROBE MICROSCOPY SYSTEM FOR USE IN
SEMICONDUCTOR NANOCRYSTAL CHARACTERIZATION

Bostancı, Umut

M.Sc., Department of Physics

Supervisor: Prof. Dr. Raşit TURAN

August 2007, 55 pages

Atomic Force Microscopy (AFM) and Kelvin Probe Microscopy (KPM) are two surface characterization methods suitable for semiconductor nanocrystal applications. In this thesis work, an AFM system with KPM capability was developed and implemented. It was observed that, the effect of electrostatic interaction of the probe cantilever with the sample can be significantly reduced by using higher order resonant modes for Kelvin force detection. Germanium nanocrystals were grown on silicon substrate using different growth conditions. Both characterization methods were applied to the nanocrystal samples. Variation of nanocrystal sizes with varying annealing temperature were observed. Kelvin spectroscopy measurements made on nanocrystal samples using the KPM apparatus displayed charging effects.

Keywords: Atomic Force Microscopy, kelvin probe microscopy, germanium, nanocrystal, Kelvin spectroscopy

ÖZ

YARIİLETKEN NANOKRİSTAL KARAKTERİZASYONUNDA KULLANILMAK ÜZERE ATOMİK KUVVET MİKROSKOBU VE KELVİN SONDASI MİKROBU GELİŞTİRİLMESİ

Bostancı, Umut

Yüksek Lisans, Fizik Bölümü

Tez Yöneticisi: Prof. Dr. Raşit TURAN

Ağustos 2007, 55 sayfa

Atomik Kuvvet Mikroskobu (AKM) ve Kelvin Sondası Mikroskobu yarıiletken nanokristal uygulamaları için uygun iki yüzey karakterizasyon yöntemleridir. Bu tez çalışmasında, KPM kapasitesine sahip bir AKM sistemi geliştirilip üretilmiştir. Kelvin kuvveti algılanmasında tınlaşım kolunun örnek ile elektrostatik etkileşiminin etkisinin, yüksek dereceli tınlama modlarının kullanımı ile önemli derecede azaltılabileceği gözlemlendi. Silisyum taban üzerinde değişik büyüme koşullarında germanium nanokristaller büyütüldü. Her iki karakterizasyon yöntemi üretilen nanokristal örneklere uygulandı. Menevişleme sıcaklığı değişimine bağlı nanokristal boyut farklılığı gözlendi. KPM kullanarak nanokristal örnekler yapılan Kelvin spektroskopisi ölçümlerinde, yüklenme etkileri gözlendi.

Anahtar kelimeler: Atomik kuvvet mikroskobu, Kelvin sondası mikroskobu, germanyum, nanokristal, Kelvin spektroskopisi

To my family

ACKNOWLEDGEMENTS

TABLE OF CONTENTS

LIST OF FIGURES

Figures

CHAPTER 1

INTRODUCTION

1.1 Review of Scanning Probe Microscopy

The needs of surface science and nanotechnology for surface imaging in nanometer scale have led to the development of scanning probe microscopy (SPM). SPM differs from the previously developed microscopy techniques for its utilization of a probe, that has microscopic dimensions itself, and scanning it over the imaged area, recording a quantity related to the probe that varies with varying surface property. In contrast, most of the previously developed methods made use of a macroscopic assembly that imaged the samples from a distance. Numerous different kinds of interaction of probe with different surface properties were utilized in imaging.

First type of SPM to be proposed was the Scanning Tunneling Microscope (STM) [1,2]. It was developed by G. Binnig and H. Rohrer of IBM Zürich Research Laboratory, the first patent disclosure being submitted in 1979. A bias voltage applied between a conducting probe tip and a conducting sample, a tunneling current establishes whose value decays exponentially with increasing tip sample separation. The tunneling current is given by [3]

$$I_t(z) = I_0 \exp(-2\kappa_t z) \qquad (1.1)$$

where I_0 is a function of bias and density of states in tip and sample, and κ_t is given by

$$\kappa_t = \sqrt{2m\Phi}\,/\,\hbar \qquad\qquad (1.2)$$

Where m is the electron mass, Φ is the work function of the tip. Using a metal tip, Φ would be around 4 eV which gives an order of magnitude drop in current when the separation increases by an angstrom.

Exponentially decaying tunnel current enables operation with good vertical resolution in atomic scale. The dominant noise source is the resistor used in transconductance amplifier to pick up the current signal. Having a high slope region in the current-separation characteristics lead to low noise level in the height signal [3]. For samples having taller structures tip height is controlled by a negative feedback loop during surface scan. The probe tip is required to have a smaller curvature as possible to increase resolution and the probe itself is rigid to avoid oscillations. Piezoelectric actuators position the probe over the surface. Atomic scale resolution in lateral directions was demonstrated at cryogenic temperatures and ultra high vacuum environment. Although presenting very high resolution, Scanning Tunneling Microscopy has drawbacks. It requires the probe and more importantly the sample to be conducting. Also, accidental tip surface contact causes modifications on both tip and the sample due to current flow.

Atomic Force Microscopy (AFM) employs a simple concept and refines it. The measured interaction is the contact force applied on the tip by the sample surface. A working system was reported in 1986 by G. Binnig, Ch. Gerber and C. F. Quate [4]. Instead of using a rigid probe as in original STM, the probe structure used by AFM features a cantilever beam that carries the tip. Figure 1.1 shows images of commercial AFM probes [5]. The tip force is transduced by measuring the associated deflections of the cantilever. Interaction of the tip with the surface can be continuous

or intermittent depending on the operating mode. Sample and probe material can be non-conducting. This is a clear advantage over STM.

Figure 1.1. Commercial AFM probes [5].

1.2 Overview of Atomic Force Microscope Operation

Atomic force microscopes themselves have different modes of operation. Contact mode AFM, which can also be called tapping mode, is the first devised operation mode. During the scan, probe tip is in continuous contact with the sample surface. Deflections of the cantilever are sensed. The stiffness of the cantilever is selected to be lower than that of the bulk atoms on the tip and the sample [3]. Interatomic force constants are in the range from 10 N/m to 100 N/m in solids and can be as low as 0.1 N/m in biological samples [3]. Cantilevers with low spring constants however have lower resonant frequencies which may limit the speed of scanning, since the topography signal bandwidth should be smaller than the resonant frequency for establishing stability. To have high enough resonant frequencies, the cantilevers with very small mass are made by micromachining.

There are a number of methods for sensing the cantilever deflection. These include the use of piezoelectric or piezoresistive materials for the cantilevers which turns probes into self contained sensors, or the use of external deflection sensors such as ones employing varying capacitance, laser interference or deflection of a beam from the cantilever backside. The sensitivity of the transducer set-up is normally better for a range of deflections. This imposes a restriction to the total vertical travel distance

allowed. Furthermore, the sensitivity may not be uniform throughout this range either, which will cause signal distortion. This problem, which also holds for many other kinds of SPM, is overcome by using a feedback control system that maintains the average deflection of the cantilever. While the sample surface is scanned, the feedback system positions the probe so that it follows the surface profile. As a result, the vertical position of the probe becomes same as the surface profile and can be used to form an image that reflects the surface topography with real scale.

Contact-mode AFM has been demonstrated with atomic scale resolution but has shortcomings. Thermal expansion of the system causes 1/f noise and this can be reduced by low-temperature operation and materials with low coefficient of expansion [3]. Presence of lateral forces applied on the sample is not preferred especially with loose surfaces such as those of organic and biological samples. Lateral forces may cause modifications in both tip and sample surface [6].

In non-contact mode AFM, the cantilever is vibrated at or near the resonance frequency, and allowed to touch the surface at the maxima of the oscillation. An advantage of this is being liberated from 1/f noise which is pronounced at lower frequencies. The ac deflection signal is mixed with a reference of the drive signal to be downconverted. The resulting signal is used in the feedback loop. The basic scheme is amplitude modulation (AM) AFM. In this scheme the cantilever is driven at a frequency near its resonance. When the tip is brought in contact with the surface, the oscillation amplitude diminishes through loss of energy due to tip continuously impacting the surface. Increase in the loss factor in the resonant system also causes phase shift in the oscillation signal. During the scan, variations in surface height cause the amplitude and phase to vary accordingly. The amplitude or phase can be used as the variable for the feedback controller input to get a true topography image [3].
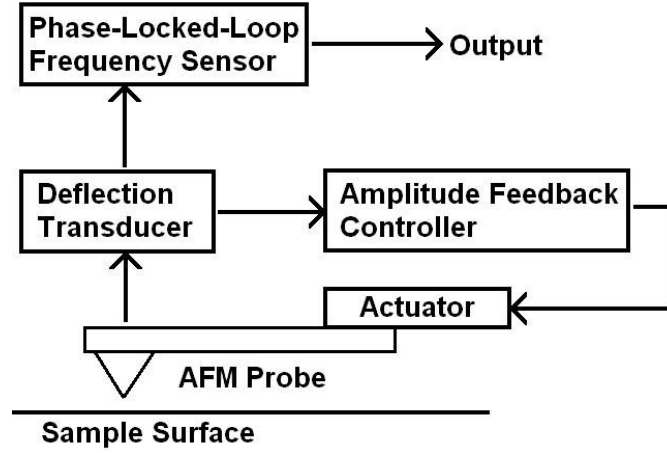
Figure 1.2. Simplified structure for frequency modulation AFM scheme.

Another scheme is frequency modulation (FM) AFM [3,7,8]. In this scheme, the oscillation frequency is not dictated by the driving signal but allowed to vary around the resonant frequency using a special driving circuit. Interaction of the probe tip with the sample modifies the effective spring constant of the cantilever by adding an external force component. The effective spring constant is related with the interaction potential by [3]

$$k' = k + \frac{\partial^2 V}{\partial z^2} \tag{1.3}$$

where V is the interaction potential. This leads to a shift in the effective resonance frequency which is related to the mass and the spring constant of the cantilever by

$$f = \frac{1}{2\pi} \sqrt{\frac{k}{m}} \tag{1.4}$$

The oscillation amplitude is also modified due to deviation of the oscillation frequency from the actual resonance frequency. Simplified configuration for FM-AFM is seen on Figure 1.2. Oscillation signal from the cantilever transducer branches into two, it is transmitted to a phase locked loop (PLL) that detects the

variation in oscillation frequency. The signal also passes through an amplitude feedback loop that keeps the oscillation amplitude constant by adjusting the drive signal but not forcing a constant frequency. This is needed since otherwise, variations in the amplitude would alter the readings from the PLL.

CHAPTER 2

ATOMIC FORCE MICROSCOPE CONSTRUCTION

2.1 Overview of the System

The AFM system used in this thesis work is developed and implemented at METU Physics Department. It is designed to be mounted in a vacuum chamber and to operate in high vacuum environment. The chamber itself is mounted next to a sputtering system and also acts as a sample loading facility for this system. This configuration allows the user to fabricate semiconductor nanocrystal samples and characterize them using the AFM without exposing them to air. There is a door on the chamber which is used for loading and unloading the samples. The samples are carried on the sputtering chamber using a rod accessible from the outside by using a magnetic holder that sticks onto the positioner stage that manipulates the samples. Figure 2.1 shows a picture of the AFM chamber

AFM Chamber   **Sputtering Chamber**
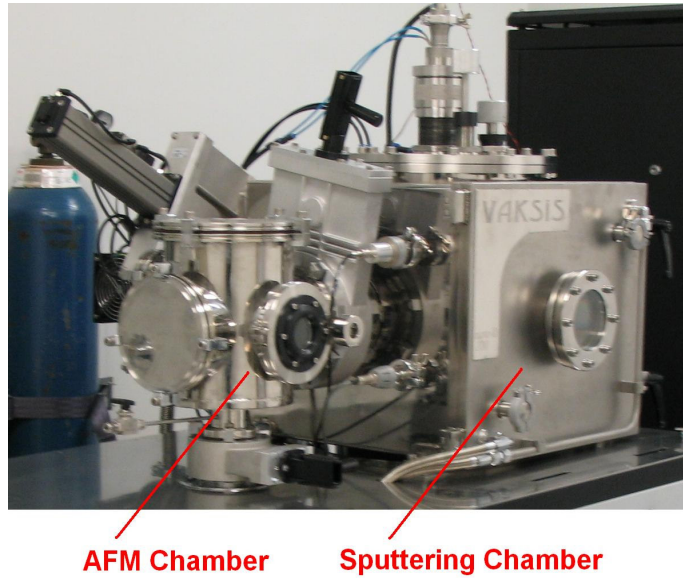
Figure 2.1. Vacuum chambers of the in-site sputtering and microscopy system.

The AFM itself is designed to be located such that the manipulator rod can pass through the system to reach the sputtering chamber. The sample mount of the system is built to be on the upper side, while the AFM probe is located on the lower. The reason for this configuration is to comply with the sputtering system configuration in which the sputtering targets are on the lower and the holder is on the upper side. This compliance between the AFM and sputtering system allows samples to be transferred from one to the other without the requirement of rotating them upside down. The system is not yet installed into the vacuum chamber by the time this thesis is submitted.
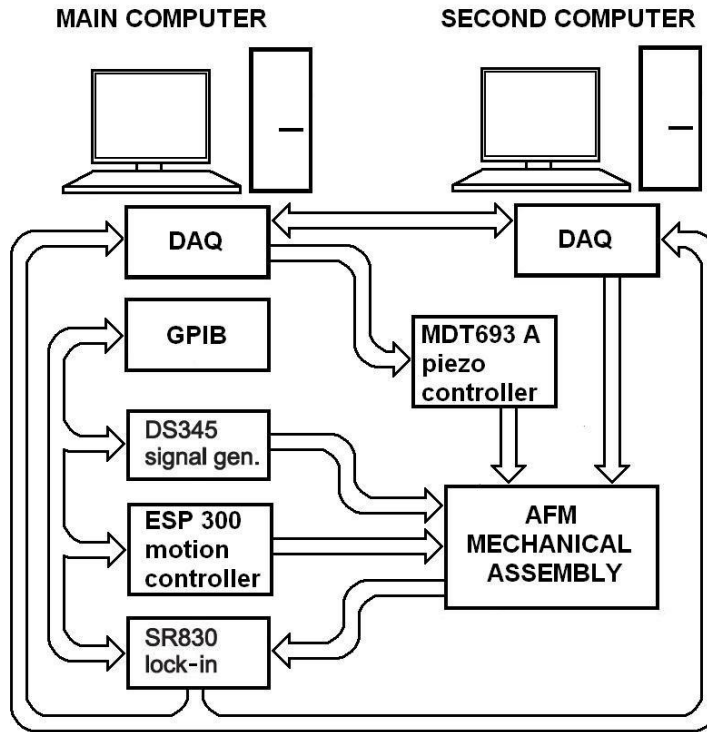
Figure 2.2. Block diagram of the AFM system.

The block diagram of the AFM is shown on figure 2.2. The AFM probe and detector assembly, the servo and piezo positioners are grouped under the name AFM mechanical assembly.

2.2 Servo Positioning

The AFM system uses three identical high precision servo positioners. Two of these positioners are mounted beneath the X-Y scanning piezo positioner stage on top of each other, used for the X-Y positioning of the sample being imaged. The other positioner carries the probe head assembly, and is used for the coarse approaching of the scanning probe to the sample surface. The positioners are Newport CCV6 dc servo motor stages [9] which are ultra high vacuum compatible. The stage features a precision dc motor, an 2048 cts/rev encoder, low friction mechanical design and a low ratio reduction gear that allows the stages to translate with 20 nm minimum steps and 50 nm sensitivity [9], with up to one kilogram of load mounted on them. The 20

nm minimum step size is more than sufficiently precise for the coarse approach for when even a high voltage amplifier is not used for driving the height piezo positioner. The maximum travel distance of the stages is 25 mm. Configuration of the servo positioners are seen on figure 2.3.
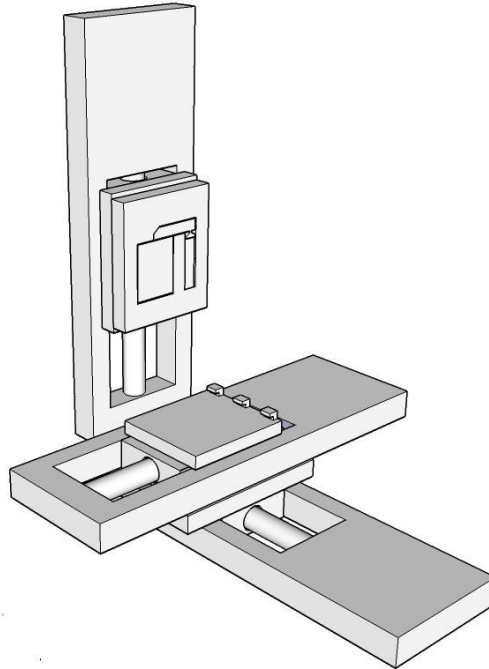
Figure 2.3. Configuration of the servo positioners.

The positioners are controlled by a Newport Model ESP300 [10] universal motion controller / driver unit. The unit communicates with the master computer using a GPIB interface.

2.3 Three Axis Piezo Positioning

SPM images are taken by scanning a probe over the surface being studied. Triple axis movement of the probe relative to the surface can be achieved by using some different configurations. In our design the X-Y positioning and scanning are done using an integrated two axis piezo stage that is mounted over the X-Y servo stage

stack beneath the sample holder. The Z positioning is done by a single axis piezo stage that is mounted on the Z axis servo positioner beneath the probe assembly.

2.3.1 Single Axis Piezo Positioner Stage

This stage was designed by Dr. Aykutlu Dâna, in the context of his Ph.D. work. Figure 2.4 shows the stage. The stage accepts a piezo actuator. The actuator is linked with the pad that the load is mounted via a third class lever, with a displacement ratio of 1:5. Maximum end to end displacement range of the stage is measured to be 30 μm. The frequency response of the stage with the piezoresistive probe mount is characterized by exiting the stage with a function generator and measuring the cantilever deflection. Fundamental resonance peak is observed at around 750 Hz. Instability in height feedback system operation due to this resonance peak should be avoided by keeping the bandwidth of the probe signal well below the peak during scan.
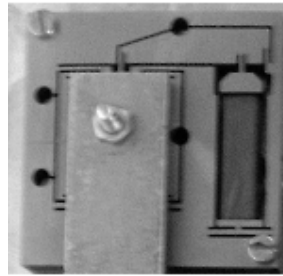
Figure 2.4. Single axis piezo positioner stage.

2.3.2 Double Axis Piezo Positioner Stage

The X-Y scanning motion of the sample is to be done by a combined double axis piezo positioner stage. A possible configuration makes use of a rectangular platform suspended inside a rectangular frame, which itself is suspended in the stationary frame.

2.4 Mechanical Considerations

During the development phase, the parts are integrated on an aluminum breadboard specially produced for the purpose. This prototype system was intended for serving through the software development. Considering the limitations imposed by the use of the breadboard, the system was simplified to have a linear design as seen on figure 2.5. The servo positioners on the sample side are omitted and replaced by a manual two axis stage. A piezo tube X-Y scanner is mounted on this stage, and the sample holder is attached to the tube's end. The probe is attached to the single axis piezo controller which is mounted on a single servo positioner. Both of them are performing the z-axis positioning.
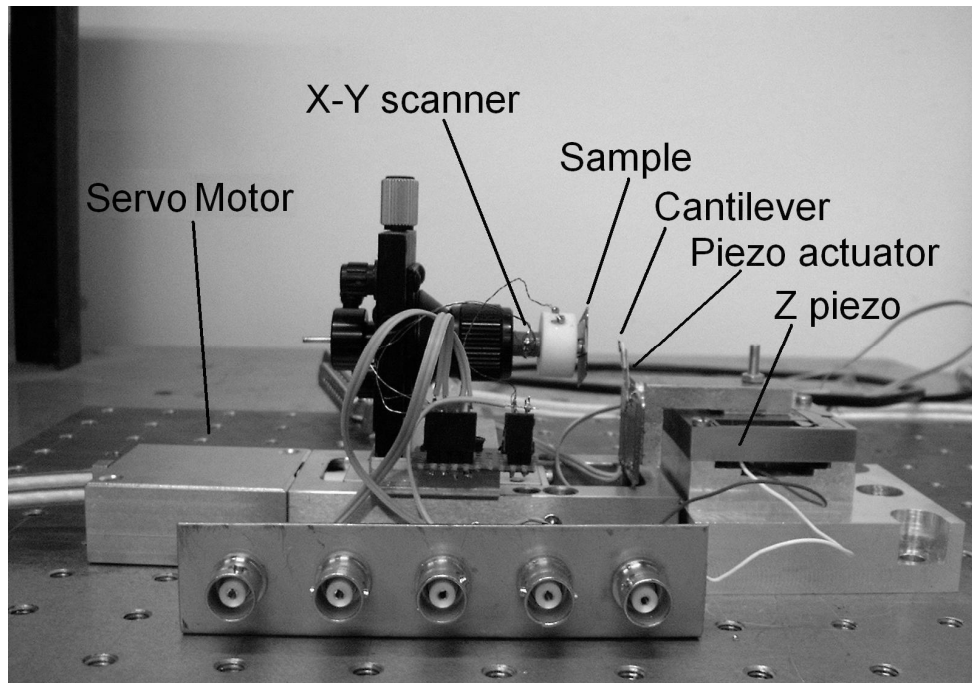
Figure 2.5. AFM prototype working in air.

Design of the vacuum system is done. Figure 2.6 shows the assembly drafts. In this design, the sample holder and the stages underneath the holder are placed downside and the probe assembly is placed up. To comply with the newly constructed loading

system, the design is going to be altered to have the sample holder upside, keeping other elements mostly unchanged.
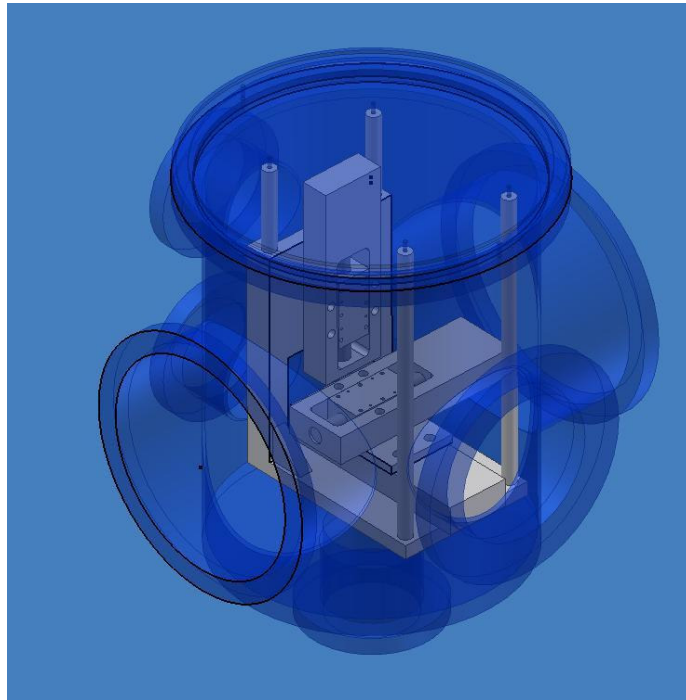
Figure 2.6. Vacuum assembly design of the system.

2.5 Cantilever Detection Subsystem

The essential element of AFM imaging is the detection of cantilever deflection. Depending on the operating mode of the AFM the deflection signals character varies. The signal can be an unmodulated one, with its value changing with the topograpy of the scanned surface in contact mode operation. Whereas in tapping mode and in other modes where the cantilever is externally driven with high frequency, the deflection signal is modulated by the driving frequency, and the information is carried by the amplitude and phase of the signal.

In contact mode operation, the deflection signal is conditioned with a dc coupled amplifier and then fed into the data acquisition board installed on the second computer, on which the topography feedback program is running.

In tapping mode and in other modes of operation which makes use of a oscillatory cantilever, the output signal, which is modulated in amplitude and phase, by the surface topography measured is fed into a Stanford Research Systems SR830 lock-in amplifier to be demodulated.

2.5.1 Piezoresistive cantilever detection

In the piezoresistive cantilever detection method, a piezoresistive device usually made of silicon is implemented on the cantilever body. Deflections of the cantilever build stress on the cantilever body and the piezoresistive element, and thus modify its resistance. The resistance value is converted to a voltage signal by the read out circuit. This method is straightforward to apply because it does not make use of optical assemblies. Providing electrical connection to the cantilever chip is necessary. This is accomplished by having the chip mounted on another substrate that has contact pads which are connected to the chip terminals by wire bonding. Shortcomings of this detection method are the inferior noise performance and the unavailability of conducting cantilevers. Signal to noise ratio of piezoresistive detection systems are more than two orders of magnitude worse than that of optical methods due to the resistor thermal and 1/f noise [11]. The cantilevers are usually made of silicon and non-conducting silicon, and the commercial availability of the probes are limited to mostly custom built products.

2.5.2 Beam deflection configuration

In this detection method, a laser beam is focused onto the reflective backside of the cantilever head, which is deflected with the angular motion of the cantilever [12]. Figure 2.7 shows a possible beam deflection configuration. The visible light from the fiber coupled laser diode is collimated by a lens A, and focused on the back side of the cantilever which is mounted on the holder C, by the lens B. The reflected light is collimated again by the lens B reflected from mirror D and sent onto the detector mounted on the circuit board E.
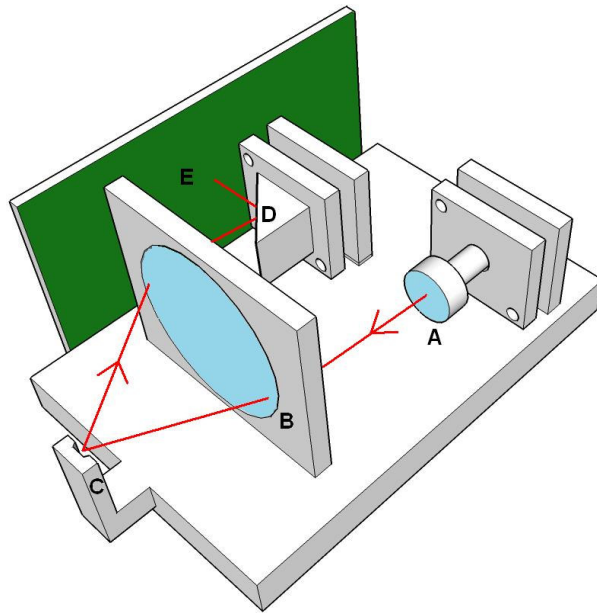
Figure 2.7. Possible configuration for a beam deflection detector.

Figure 2.8 shows the analysis of the optical system carried on Raytrace optical analysis software. For simplification, mirror D on the above configuration is omitted. The effect of changing the cantilever angle is shown on A and B, and the effect of changing the cantilever distance are shown on B and C. According to this analysis, the detector can be placed so that, the effect of change of distance is minimized. The angular movements of the cantilever cause the final beam to translate in the direction of the rotation. An advantage of this design is that it is less sensitive to the translational displacement of the cantilever. This is expected to reduce the effects of expansion and contraction due to temperature variation on the performance.
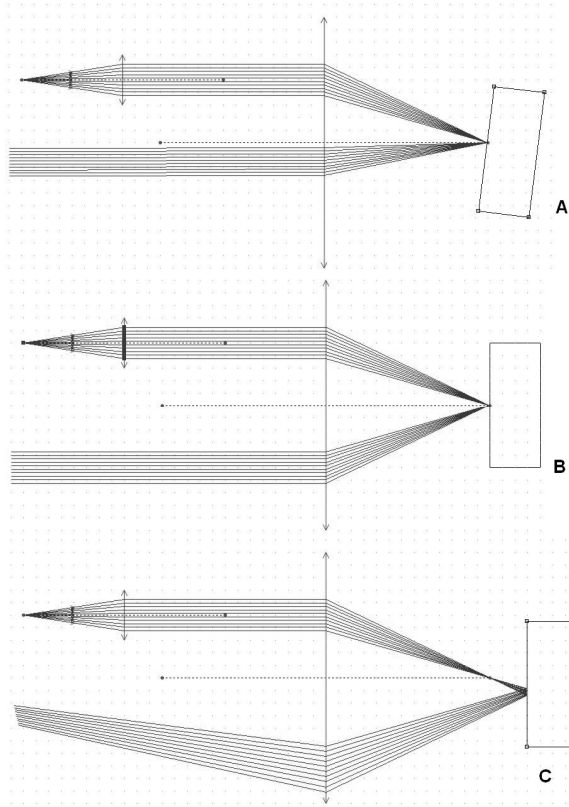
Figure 2.8. Analysis of the beam deflection system.

2.5.3 Laser Interferometer

Optical interferometry has been widely used in the detection of small movements [13]. Figure 2.9 shows the configuration of a laser interferometer deflection detector. These systems are usually implemented using fiber optics to reduce the probe head assembly weight and to avoid alignment difficulties. The fiber coupler shown on figure acts as a beam seperator, coupling the laser output to the cavity and steering the reflected beam to the detector. The cavity itself is a Fabry Perot type interferometer with one reflector being the end of the fiber and the other the reflecting back side of the cantilever. For cavity lengths sufficiently smaller than the coherence length of the laser, intensity of light reaching the detector can be expressed as [13]

$$I = 2I_0 \left(1 + \cos\left(\frac{4\pi}{\lambda} x + \phi_0 \right) \right)$$

<div align="right">(2.1)</div>

Where I_0 is the laser output intensity, x is the distance between the fiber end and the cantilever and ϕ_0 is a constant phase term. The fiber end placed close to the cantilever backside, and is aligned to assure a reasonable amount of reflected light is coupled back to the fiber. The equilibrium distance of the cantilever to the fiber is adjusted so that the variation of intensity of the light reflected back from the cavity is maximized. The width of the fringes is half the wavelength of the light used. The dynamic range of the interferometer is around this value halved because the sinusoidal variation of the intensity with distance. Using a 1310 nm source will result in a dynamic range of around 325 nm. The laser output level is optimized to have the highest possible intensity without driving the laser in to mode-hopping regime.
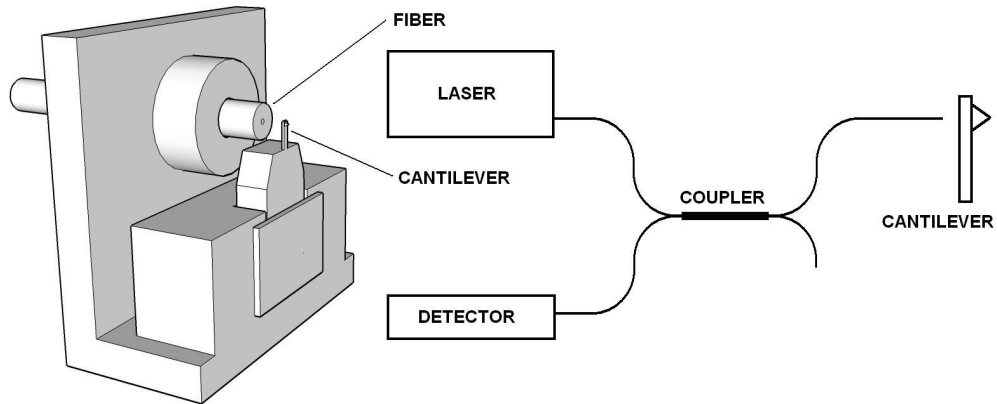
Figure 2.9. Sketch and block diagram of fiber interferometer.

2.6 Control and Imaging Hardware and Software

A block diagram of the control and imaging hardware is shown on figure 2.1. There are two computers on the system. The main computer controls the servo positioners and the scanning piezo positioner. It also controls the function generator and the lock in amplifier and collects the imaging data and serves as the user interface. There is a National Instruments GPIB interface board and a National Instruments PCI-6221

data acquisition board installed on the main computer [14]. The second computer runs the topography feedback program and is controlled by the main computer via a communication channel in between. Another National Instruments PCI-6221 data acquisition board is installed on the second computer.

For amplitude and phase detection a Stanford Research Systems SR830 lock in amplifier is used. This unit is a two channel heterodyne detector implemented fully on a digital signal processor. This provides the device increased robustness over analog lock-ins in terms of calibration. A Newport ESP300 universal motion controller / driver unit controls the servo positioning stages. The unit has a GPIB interface. The piezo positioners are driven by a Thorlabs MDT693A triple axis piezo controller. The unit can be controlled by its RS232 interface or directly from its analog inputs.

2.6.1 Main Computer

The main computer has a Pentium 4 CPU, 1024 megabytes RAM, with a National Instruments GPIB controller board and a National Instruments PCI-6221 data acquisition board. The main program is running on this computer and the user operates the system fully from here. The data acquisition board has 16 analog inputs with 250 kS/s 16 bit converters, 2 analog outputs with 833 kS/s 16 bit converters and 24 digital I/O channels. Four of the analog input channels collect imaging data, and the two analog outputs are driving the high voltage amplifier which generates the X-Y piezo scanner voltages.

The main computer communicates with the second computer via a digital communication channel established using the digital I/O channels on the data acquisition boards installed on each computer. The communication channel is one way from the main to the second computer.

2.6.2 Software running on main computer

The program running on the main computer is developed on Delphi 6.0. This program generates the X-Y scanning signals for the piezo controller, collects, processes and displays the imaging data, and adjusts the settings of the other components and the feedback program running on the second computer. The user interface is shown on figure 2.10. Wide window on the left displays the raw image. The other window has three tabs. Scanner controls are on the first tab. The second tab displays the controls for piezo actuator parameters. The third tab is an interface for the feedback program running on the second computer.
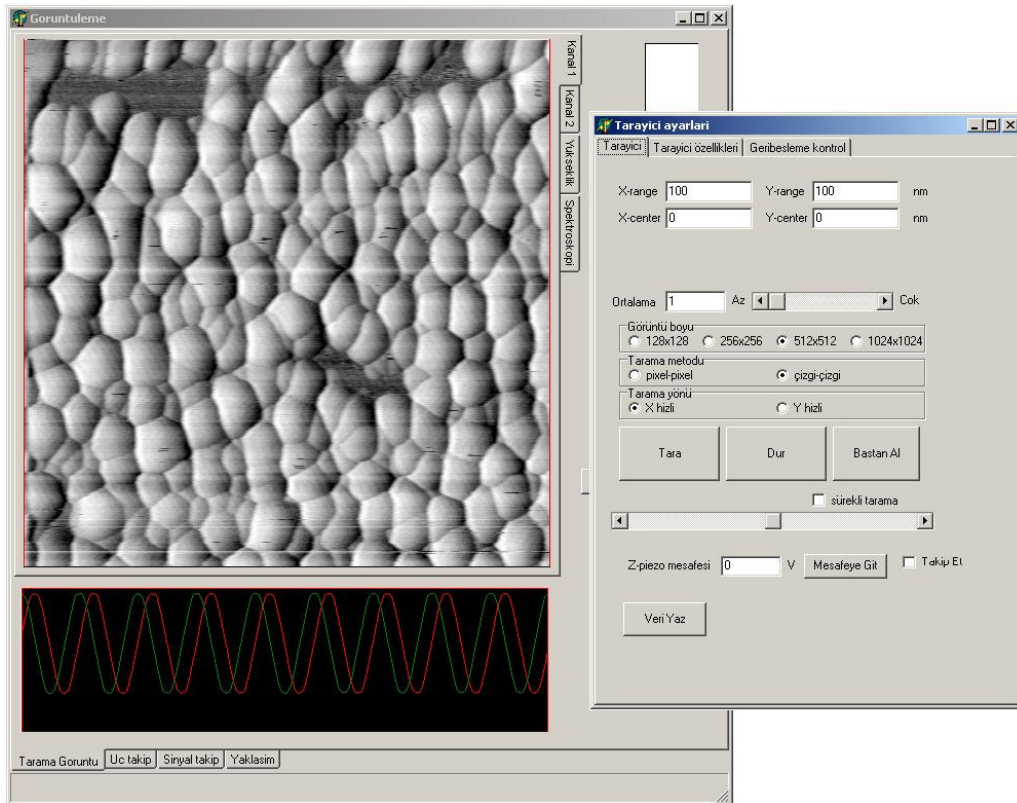
Figure 2.10. AFM main program user interface.

Four data channels are sampled simultaneously and can be displayed during imaging. Data points are averaged during the scanning with variable number of averaging points. The scanning span and center point is instructed and the fast scanning

19

direction can be selected as X or Y axis. While imaging, each line is scanned forward and backward. The forward scan data is used for constructing the raw image and each line is fitted linearly within itself. The raw data is exported to be processed later.

The scanning speed, which is the time needed to complete an image, is limited by the scanning loop execution time. When the sample is scanned by speeds lower than the maximum possible, each image point is averaged to improve the signal. Typically a 1μm × 1μm area image is completed in 5 minutes, when scanned by taking a reasonable number of averages to reduce the noise in the final image.

2.6.3 Software running on second computer

The elementary component of the topography feedback subsystem is the PID controller that generates the feedback signal. For use in the AFM system, the parameters of the controller have to be adjustable to obtain the best performance with various surface properties. Also it should be possible to shut down the controller, and also to manipulate the Z axis piezo positioner manually. To match these needs, the controller is implemented on the second computer. Two of the analog input channels of the data acquisition board installed on the computer are used as signal inputs, and an analog output channel is used for outputting the control signal for the Z axis piezo positioner. Eight digital I/O channels are used for establishing the digital communication channel with the main computer.

The two input channels digitize the in phase and quadrature components of the complex envelope of the cantilever signal outputted by the lock-in amplifier. Using these two inputs, four different feedback input signals are generated by the feedback program. These are the detected signals in phase component, quadrature component, amplitude and phase. The input signal selection is made from the main program running on the main computer.

The feedback program regularly polls for commands coming from the main computer. The commands consist of four words of six bit each transferred through the six of the digital I/O channels of the DAQ board. Two digital channels are employed as flags for regulating the communication. One of them is the write flag of the main computer that is set high when there is a command, the other one is the read flag of the second computer that is set when the command is read and the program is ready for a new command. The first word of the command is the code for the operation to be performed. The remaining words are used for transmitting a numerical value.

CHAPTER 3

APPLICATION OF AFM TO NANOSTRUCTURED SURFACES

The system was used for taking images of some samples with micrometer and nanometer scale features. The purpose was to characterize these samples and also test the system performance during the development. The configuration used for the development worked with piezoresistive probes.

3.1 Holographic Gratings

Holographic gratings were used as test samples during the development of the system. The gratings were produced and kindly supplied by Mr. Aşkın Kocabaş. They were produced by photolithographic process using an expanded laser beam interfered on the surface with part of itself reflected from a mirror [15,16]. The pitch of the gratings was around 1.1 μm. A topographical scan of a grating taken by the AFM system is shown in figure 3.1. The non-symmetrical structure of the grating is revealed on the image. The features are softened to due to the worn tip. Some color banding is visible in the image; these bands indicate drifts in the system due to changing temperature. The image is corrected by adding a term which is linearly varying with the x and y coordinate. This correction was done in order to eliminate the effect of the angular tilt of the sample with respect to the scanning plane. The color banding can also be corrected by adding higher order terms in x and y coordinate. Such a correction, however is not done on this image.
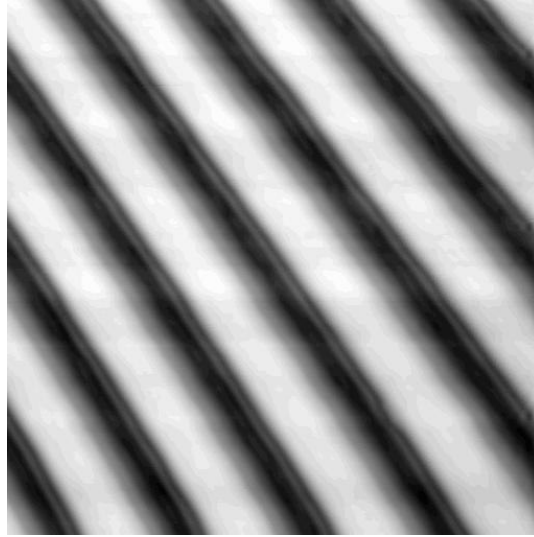
Figure 3.1. Topography image of a holographic grating.

3.2 Germanium Nanocrystals on Silicon Surface

Nanocrystals of germanium can be formed on silicon surface. Difference between bulk bandgaps is 0.46 eV. Discontinuity formed at the hole band in a heterojunction formed between the two materials is 0.39 eV on average [17]. Holes can thus be confined in the germanium nanocrystals on the surface due to this discontinuity. The nanocrystals are formed on a silicon surface if the surface is coated with a thin layer of germanium under suitable conditions. Formation of the nanocrystals are attributed to Stranski-Krsatanow growth mechanism. Having a bulk lattice parameter larger than that of silicon, germanium starts to form a strained layer over the surface. As the layer gets thicker than few monolayers, the high layer energy due to the strain is relaxed by forming dislocations. Germanium continues on to grow in islands around these dislocations [18,19].

Samples with different coating thicknesses were prepared. For all runs, the substrates were prepared by ultrasonic cleaning in pure acetone and removing the native oxide layer in dilute HF solution. On the first run, a 10nm layer of germanium was deposited by sputtering on a (100) p-type silicon substrate heated to ~ 200 C° to promote surface mobility. The substrate was baked at around 500 C° for half an hour

in high vacuum condition for further surface cleaning. The film was then in-situ annealed at around 500 C° for an hour and scanned on the AFM system. Figure 3.2 shows the phase image taken from a 1μm × 1μm area.
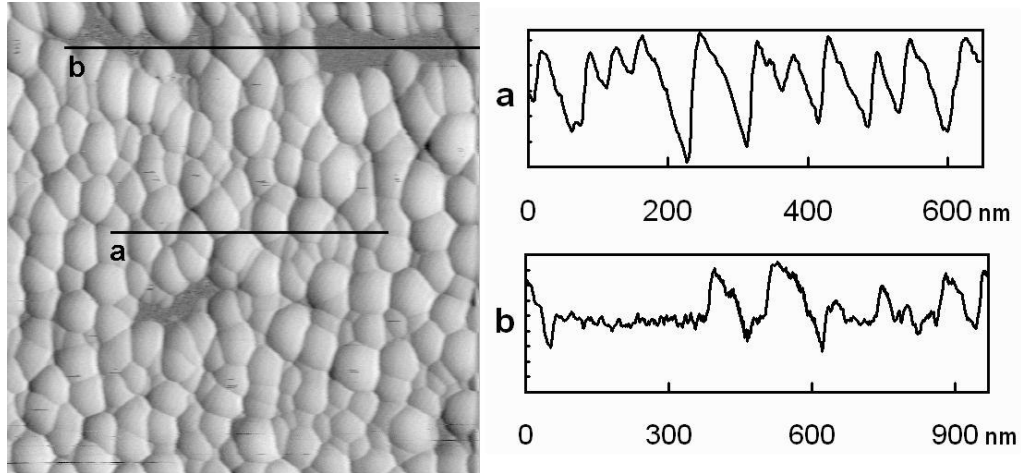
Figure 3.2. Image of sample from the first run. Scanned area is 1 μm × 1 μm.

Average nanocrystal diameter calculated from trace a on Fig. 3.2 is 57 nm. Trace b on Fig. 3.2 shows a section from line b indicated on the image. The flat region can appears to be the substrate. The nanocrystals formed are adjacent to each other over most of the imaged area.

The second and third runs were carried using a different method to achieve a true Stranski-Krastanov (SK) mode of island formation. Instead of post annealing the samples, the substrate temperature during sputtering is raised to the range of annealing temperatures. P-type silicon substrate was cleaned and coated with a layer of germanium by sputtering with a thickness of around 2 nm. The substrates were held at around 500C° to promote the island formation during coating. The samples were then cooled and scanned with the AFM system. Figure 3.3 shows two different images taken from 1 μm × 1 μm areas on the sample from third run.

24
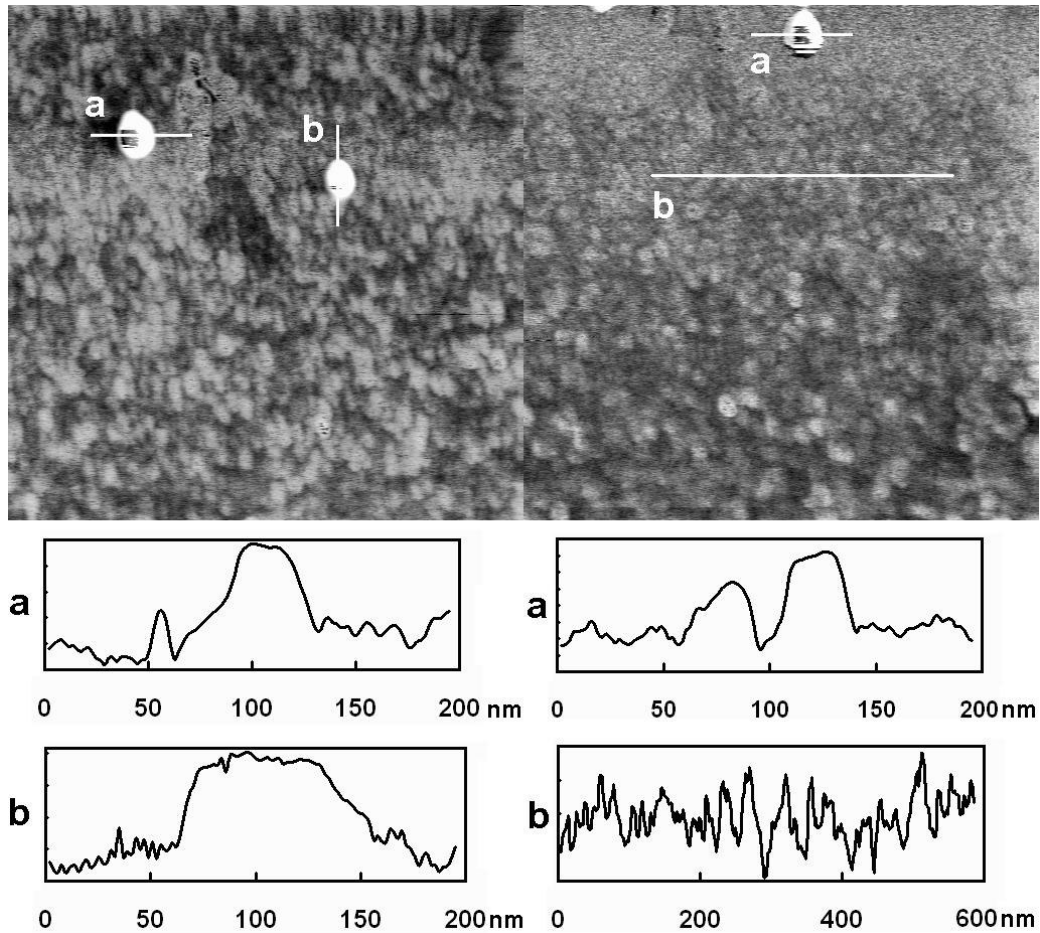
Figure 3.3. Images of the sample from 3rd run showing isolated high regions together with shallow ripples. Plots showing sections as indicated on figure. Scanned areas are 1μm × 1μm each.

The images show three isolated high regions with average diameter of 85 nm. The remaining area is occupied by shallow structures with diameters ranging from 8 nanometers up to 50 nanometers. The isolated regions are suspected to be germanium islands.

The fourth run was a return to the original method. A p-type substrate was baked at ~ 500 C° for half an hour at high vacuum after the cleaning procedure. It was then sputter coated with a 5 nm germanium layer being held at ~ 200 C° and in-situ annealed for half an hour at around 500 C°. A thinner layer when compared to the

first run was coated to produce islands that are separated from each other. Figure 3.4a shows a 1 μm × 1 μm image of the sample. The elongation of the patterns is due to deformation of the probe tip. Figure 3.4b shows another image of the sample taken using a commercial AFM system (PSIA XEI100E) [20]. It can be seen that the surface is covered by similarly sized nanocrystals. The nanocrystals are not separated from each other. Average nanocrystal diameter was measured as 95nm from the trace.
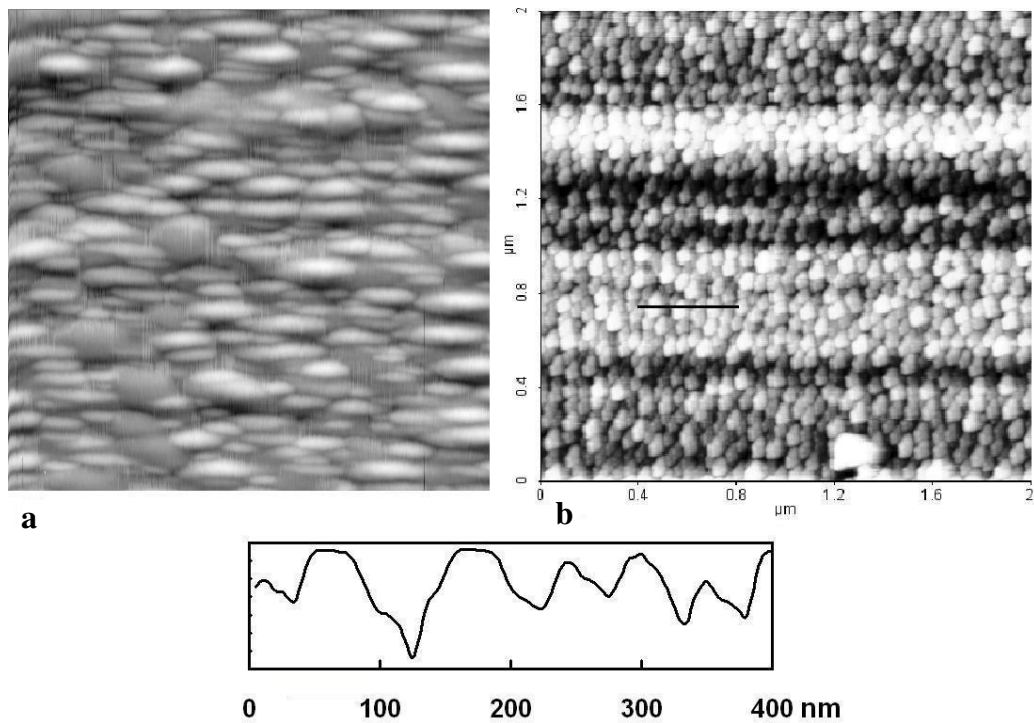
Figure 3.4. Images of the sample from 4th run.

On the fourth run, a p-type silicon substrate was cleaned with the procedure described and coated with a 5 nm layer of germanium with substrate held at room temperature. The substrate was then diced and a sample was loaded into METU Central Lab XPS facility. The sample was annealed inside the XPS chamber held at ultra high vacuum for 45 minutes maintaining a temperature gradient on the sample. Surface temperature was measured using a pyrometer from outside the XPS chamber through a transparent window. Measurement of the temperature of different regions

on the sample could not be achieved due to the wide measurement spot size of the pyrometer used. The temperature of the highest temperature region on the sample was measured to be around 700 C°. Figure 3.5a shows a topographical scan of the sample taken from a high temperature region using the commercial system. The region features isolated microscopic germanium crystals with diameters ranging from 250 nm to 450 nm. The nanocrystals are separated from each other as desired but their large average size is a drawback since they may not be suitable for modeling charging effects for flash memory applications. The color bands on the figure are due to probe head assembly drifting in large area scans.
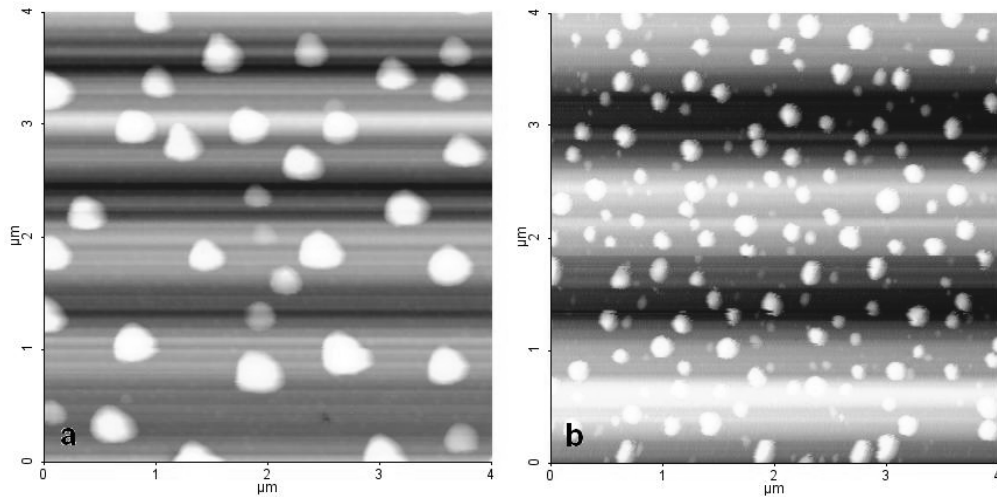
Figure 3.5. Topography images of the sample from 5th run taken from a) a high temperature region and b) a lower temperature region showing the island size variation.

Figure 3.5b shows another topographical scan from the sample taken from a lower temperature region. The germanium structures are still isolated from each other, but the average diameter is smaller with respect to the high temperature region. Lower surface mobility of germanium atoms at lower temperature may have caused less accumulation at the growing crystals.
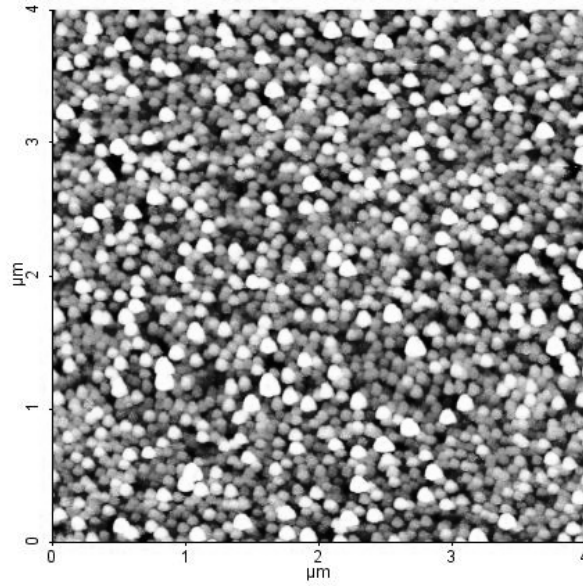
Figure 3.6. Topography image of sample from 5th run taken from a low temperature region.

Figure 3.6 shows a topographical scan of a yet lower temperature region featuring smaller islands with diameters 120 nm on average that are apparently adjacent to each other. The nanocrystal formation in this region is similar to those on samples from the first and the fourth run, suggesting the temperature in the region to be near 500 C°.

CHAPTER 4

KELVIN PROBE FORCE MICROSCOPY

4.1 Kelvin Probe Spectroscopy

If a conducting probe is brought to a close proximity of a conducting or semi-conducting sample surface, a potential difference develop between two surfaces. This is due to the work function difference between the two materials and the corresponding energy difference of electron Fermi levels with respect to the vacuum level [21,22]. Figure 4.1 illustrates this effect.
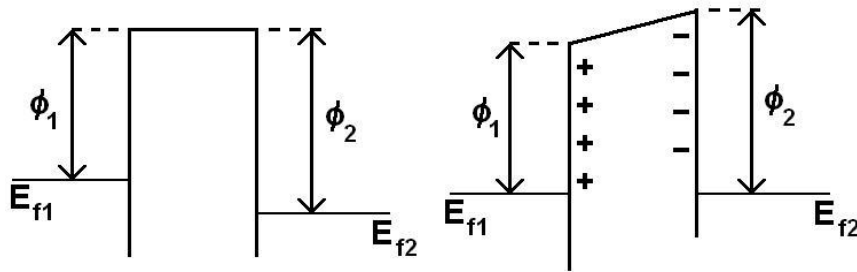
Figure 4.1. Materials 1 and 2 with different work functions ϕ_1 and ϕ_2 are brought together. The Fermi levels are then aligned by building charge on the surfaces.

The potential drop causes charge to accumulate on the probe and the sample surfaces. In reality the contact potential difference depend on parameters other than work functions as well such as oxide layers, adsorption layers, dopant concentration

in semiconductors and temperature changes on the sample [23]. Measuring the accumulated charge, the potential drop thus the contact potential difference is found.

Direct measurement of accumulated charge is not straightforward since time integration of relatively small currents is needed. An alternative measurement scheme is to vibrate the probe vertically above the surface, and measure the alternating current flow through the probe. The fundamental sinusoidal component of the current will be [21]

$$I = (V_{cp} - V_b)C_0 w \frac{d_{up}}{d_{down}} \sin(wt + \phi) \tag{4.1}$$

where V_{cp} is the contact potential difference, V_b is the externally applied dc bias voltage, C_0 is the capacitance value at equilibrium distance, w is the frequency of oscillation, d_{up} and d_{down} are the extremum distances of the probe from the sample surface and ϕ is an arbitrary phase factor. The current is nulled for a value of bias voltage, which cancels the contact potential difference. Sweeping the bias and determining the point where the current is nulled gives the contact potential difference [21].

While the principle above uses a parallel plate capacitor to model the probe surface system, in reality it is possible to use a probe with finite extension which will enable local measurements [21].

4.2 Kelvin Probe Force Microscopy

Kelvin Probe Force Microscopy (KPM) was demonstrated by Weaver and Abraham in 1990 [24]. It extends the Kelvin Probe method to be used in a scanning probe microscope configuration. The result is a nanometer resolution microscope with electrostatic measurement and imaging capability. In the method described by the authors, a sinusoidal bias voltage with a dc offset is applied between the surface and

the conducting SPM tip. An electrostatic force is then built on the tip due to the capacitance between the tip and the surface. It is given by [24]

$$F = -\frac{(V_0 + V_1 \sin(wt))^2}{2} \frac{\partial C}{\partial z}$$ (4.2)

Where again V_0 and V_1 are the dc and amplitude of the ac component respectively of the total potential difference, C is the capacitance between tip and surface and w is the frequency of oscillation. The term V_0 contain the dc offset value of the external bias voltage and the contact potential difference. The square term can be expanded

$$V_0^2 + 2V_0V_1 \sin(wt) + \frac{V_1^2}{2}(1 - \cos(2wt))$$ (4.3)

Driven by this electrostatic force, the time function describing the probe oscillation will be related to this force which can be extracted using a detection mechanism and a heterodyne downconverter. For a value of the dc offset that equals the contact potential difference, the voltage V_0 will be nulled and hence the sin(wt) term in the force expression [24,25].

This technique has some advantages over the vibrational capacitor technique discussed in the previous section. One advantage is the simultaneous use of force feedback that tends to keep the tip- surface-spacing constant. The sensitivity of the technique is claimed to be better than that of the vibrational capacitor technique and single units of charge have been detected. An important advantage over the vibrational capacitor method is the improved lateral resolution. In the vibrational capacitor technique, the probe current reduces as the tip dimension decrease. In the force based technique, the main limit is the cantilever thermal vibration which is independent of tip size [25,26].

4.3 KPM Operation

A Kelvin Probe Microscope system can be constructed starting with an AFM or a more generalized SPM system. For a KPM operation, bias voltages are needed to be applied both to the sample and to the probe. One or two lock-in amplifiers are used for the heterodyne detection of the cantilever signal at the bias voltage frequency and its first harmonic. A programmable PID controller can be used as a feedback system for nulling the fundamental frequency signal.
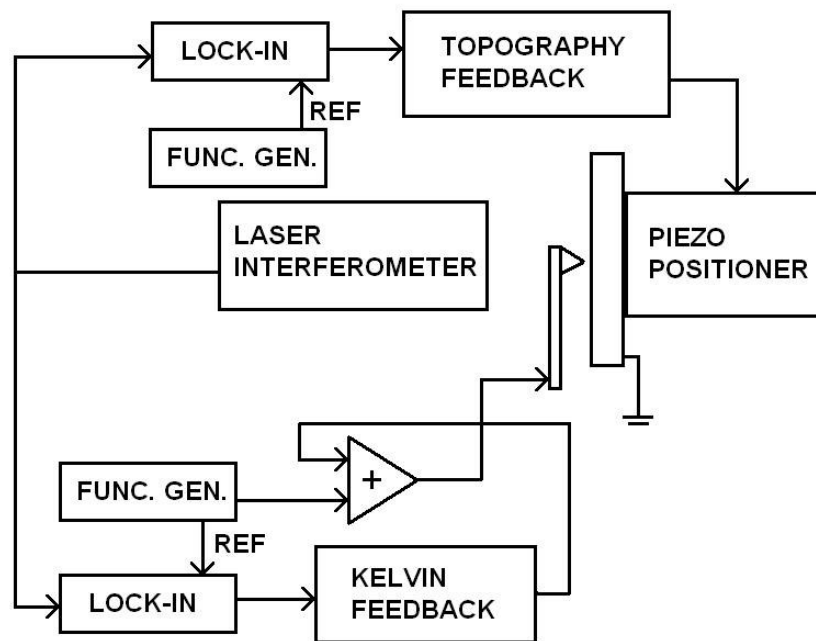
Figure 4.2. Configuration of a possible KPM system [23,25].

Figure 4.2 shows the configuration of a possible KPM system [23,25]. The cantilever is driven mechanically with a frequency near its resonance peak. The oscillation of the cantilever is transduced by a laser interferometer. The drive frequency component of the transduced signal is detected by a lock-in amplifier locked to the mechanical drive signal and is fed into the topography feedback controller as in a standard AFM system. The transduced signal is also fed into another lock-in amplifier which is locked to a signal generator which applies a sinusoidal bias

voltage to the cantilever. This generator can be set to a much lower frequency than the resonance peak. The detected signal is fed into a PID controller and the output is added to the sinusoidal bias voltage. This dc bias voltage cancels the contact potential difference. The parameters of the PID controller are to be adjusted so that the drive frequency component is effectively nulled for the potential variation of the sample surface and the scanning speed.

4.4 Resolution

The resolution of the KPM system is characterized by the electrostatic coupling between the probe tip and the surface features that at close proximity [27]. Figure 4.3 shows the model used by Jacobs et al. to estimate KPM resolution. There are capacitive elements between the tip and the surface features as well as between the surface features themselves. The electrostatic force between the tip and the sample surface can be modeled as

$$F_z = \frac{1}{2}\left[\sum_{i=1}^{n-1}\left(\sum_{j=i+1}^{n}\frac{\partial C_{ij}(z)}{\partial z}\left(\Phi_i - \Phi_j\right)^2\right)\right] + \frac{1}{2}\sum_{i=1}^{n}\frac{\partial C_{it}(z)}{\partial z}\left(\Phi_i - \Phi_t\right)^2 \qquad (4.4)$$

where F_z is the tip force, Φ_i, Φ_j, Φ_t are the potentials of the ith and jth surface feature and the tip respectively, $C_{ij}(z)$ is the capacitance between the ith and jth surface features and $C_{it}(z)$ is the capacitance between the ith feature and the probe tip. Figure 4.3 depicts the capacitance model.
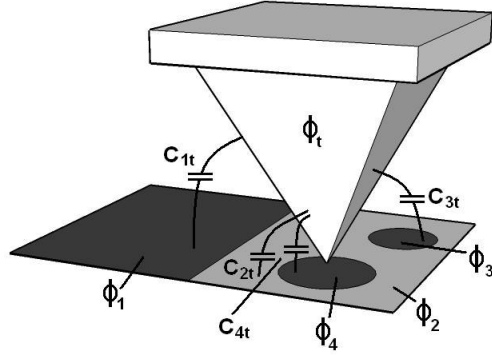
Figure 4.3. Capacitance model for KPM.

In KPM operation a driving voltage with an ac component at a frequency ω and a dc component is applied between the tip and the sample. The interaction force will then have components at zero frequency, at ω and at 2ω. The ω component is nulled by the feedback controller by applying a dc bias which can be derived to be as follows:

$$\Phi_{DC} = \frac{\displaystyle\sum_{i=1}^{n} \frac{\partial C_{it}(z)}{\partial z} \Phi_i}{\displaystyle\sum_{i=1}^{n} \frac{\partial C_{it}(z)}{\partial z}} \tag{4.5}$$

According to this equation the bias which nulls the contact potential difference hence the ω component of the tip force is determined by the combined effect of proximate surface features. The potentials Φ_i of the features contribute to the resulting estimate for the surface potential weighted by $\partial C_{it}(z)/\partial z$.

A computer program is used to determine the derivatives of the capacitances for different cantilever and tip geometries [27,28]. Probes with different geometries are also experimented. The results show that if the tip is too sharp, the contribution of the cantilever body gains importance in the resolution. The best performance was attained by using long and small cone angled tips with a slightly blunt point and a cantilever with minimal width and surface area.

4.5 Kelvin Probe Force Gradient Microscopy

The same configuration of a Kelvin Probe Microscope can be operated in the force gradient mode. In this mode, the gradient of the electrostatic force is tracked rather than the force itself [29]. Using the second order differential equation of motion for the cantilever, the amplitude and phase of the vibration can be written as [29]

$$A(\nu) = \frac{A_{res}}{\sqrt{1+Q^2\nu^2}} \quad , \quad \phi(\nu) = \arctan(Q\nu) \qquad (4.6)$$

where ν is the reduced frequency characterizing the distance from the resonance frequency and defined as $\nu=(\omega_d^2 - \omega_0^2)/\omega_d\omega_0$ where ω_d is the drive frequency and ω_0 is the resonance frequency, A_{res} is the amplitude at resonance, and Q is the quality factor of the cantilever. In case of a constant force gradient, the effective cantilever spring constant is modified, shifting the resonance frequency downwards causing the reduced frequency to shift in turn by an amount of: $d\nu$ = gradF/k_0. This causes a shift in the amplitude and phase of the cantilever vibration and hence in the output signal. The phase variation is highest when working at resonance frequency ($\omega_d = \omega_0$) and is given by [29]

$$\eta(d\nu) = \left[\frac{Q}{k_0} gradF\right] \qquad (4.7)$$

where k_0 is the cantilever spring constant. As in the KPM mode, the probe is also biased by a voltage having dc and ac components and the force gradient has components at dc, the bias signal frequency and at double frequency.

It is stated that the best performance is attained when the tip is held at constant mean distance from the surface and the amplitude of oscillation being much smaller compared to this distance. This will assure the force gradient to be nearly constant. To achieve this, the data is taken in two passes for each line of the sample scan. In

the first pass the topography of the surface is stored, in the second, the tip is held at a constant height while scanning [29].

4.6 Application of KPM

A KPM system is constructed using an existing AFM system in use at Bilkent University Department of Physics. The system used is a PSIA XE100E model which operates in air. The commercial system has auxiliary inputs to digital analog converters and output from the beam deflection detector. Both the sample holder and the probe can be biased internally or externally.
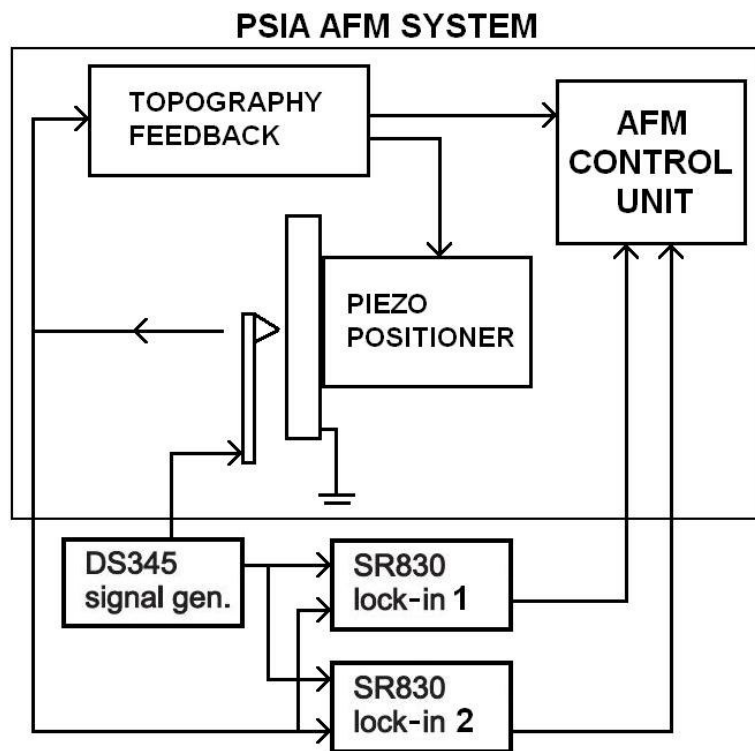

Figure 4.4. KPM system developed from commercial AFM system.

The equipment added on the system is two Stanford Research Systems (SRS) SR830 lock-in amplifiers [30], a SRS DS345 synthesized function generator [31], and a SRS SIM960 programmable PID controller [32]. Figure 4.4 shows the configuration. A 25

kHz sinusoidal drive signal with a dc offset is generated using the function generator and applied to the probe. The probe oscillation signal available from the output is applied to the both lock-in amplifiers with one of them being locked to the first harmonic of the drive signal reference and the other one to the second. In the first configuration studied, the signal phase outputs of these lock-in amplifiers were applied to the auxiliary inputs of the commercial AFM system where they were displayed and saved to be processed. In the second configuration, the amplitude output from the first harmonic lock-in amplifier is fed into the PID controller, and the output was added to the drive signal to null the first harmonic signal in the output. The PID controller parameters were set accordingly to effectively null the signal. The output of the controller was also connected to an auxiliary signal input to be displayed and saved.

The microscope was applied to a sample with germanium nanocrystals. The sample substrate was a p-type silicon wafer. The substrate was first cleaned with pure acetone with application of ultrasound, and then processed in diluted HF solution, which eliminates the native oxide layer. A 5 nm germanium film was coated onto the substrate using sputtering. The thickness of the coated layer is adjusted by varying the duration of the coating time and using a growth rate that was previously characterized by measuring a calibration layer grown with the same system. The substrate was diced and a sample of dimensions 10 mm x 10 mm was annealed in vacuum environment for 45 minutes. The heating was non uniform causing temperature variation over the sample. This caused the size of the formed nanocrystals to vary over the sample.

CHAPTER 5

MULTIMODE KELVIN PROBE FORCE MICROSCOPY

5.1 Overview

The resolution and contrast in KPM is limited by the probe tip geometry. To enhance the resolution it is desirable to achieve a small average tip sample separation and minimized interaction of the cantilever body with the sample. Maintaining small but stable tip sample separations can be difficult while the tip is biased with respect to the sample, because of the instabilities caused by the modifications of the tip and the sample. Use of a thin dielectric coating on the tip can avoid this problem. Reducing the cantilever interaction can be achieved by using the higher order resonant modes of the cantilever [33].

In multimode KPM, the second or higher resonant modes of the cantilever is used for the measurement of the electrostatic force, and the fundamental mode is used in the topography feedback loop. The mode shapes of the higher resonant modes contain intermediate nodes, and smaller tip linear displacements are associated with higher angular displacements, enhancing the transduced signal. Another advantage of having intermediate nodes is that these mode shapes consist of alternating sections which have displacements in the opposite direction to each other. This causes the electrostatic interaction between the cantilever and the sample to reduce since the capacitance variations caused by the oscillatory motion of adjacent segments tend to

cancel out. This effect is more prominent in even resonant modes in which the opposite moving segments are paired without leaving any unpaired one.

5.2 Resonant Modes and Lumped Electrostatic Interaction

The quantity to be observed in order to characterize the contact potential difference is the electrostatic interaction between the probe and the sample. The total electrostatic force acting on the probe consists of the forces acting on the tip and the cantilever body. The force acting on the cantilever body is distributed over the length of the cantilever. For making comparison with the force on the tip, the force on the cantilever body can be modeled as lumped force acting at the position of the tip apex. This lumped force is given by

$$F_{lumped,n} = \int_0^1 h_n(q)dF_{d,n}(q) \tag{5.1}$$

where n is the number of the resonant mode, q is the normalized position on the cantilever body with q = 0 indicating base and q = 1 indicating the tip and $h_n(q)$ is the normalized mode shape [34].
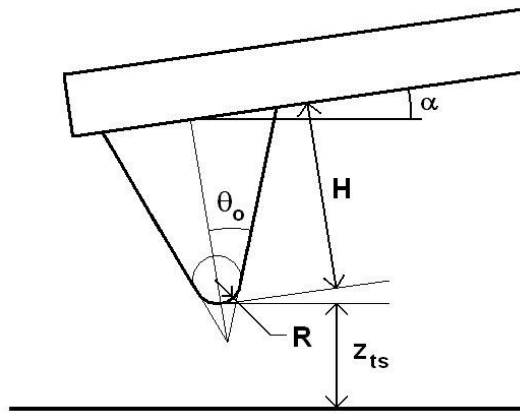

Figure 5.1. Model for cantilever body and tip [35].

Assuming that parallel plate capacitors formed between infinitesimal rectangular segments of the cantilever surface and those of the sample surface are responsible for the force, the lumped force can be calculated. Figure 5.1 shows the model used [35]. The position varying distance between the inclined cantilever and the sample is given by

$$Z(q) = z_{ts} + H \cos \alpha + L(1-q) \sin \alpha \qquad (5.2)$$

where z_{ts} is the distance between conductive tip and surface, H is the height of the tip cone, L is the length of the cantilever and α is the cantilever inclination angle. Using this, the lumped electrostatic force acting on the cantilever body can be calculated for the resonant mode n as [35]

$$F_{lumped,n} = -\int_0^1 \frac{\varepsilon_0 w L \Delta V V_{AC} \cos(\omega_n t) h_n(q) dq}{[z_{ts} + H \cos \alpha + L(1-q) \sin \alpha]^2} \qquad (5.3)$$

where, w is the width of the cantilever body, $\Delta V = V_{DC} - V_s$, V_s being the surface potential and V_{DC} being the dc component of the tip bias, and V_{AC} is the ac component of the tip bias.

Electrostatic force acting on the tip itself can be modeled by a hyperboloid tip as [36]

$$F_{tip} = -\frac{2\pi\Delta V V_{AC} \cos\omega_n t}{\left[\ln\left(\tan\dfrac{\theta_0}{2}\right)\right]^2} \left[\ln(1 + H / z_{ts}) - \frac{H\left(z_{ts} - \dfrac{R}{\tan^2(\theta_0)}\right)}{z_{ts}(H + z_{ts})}\right] \qquad (5.4)$$

where, θ_0 is the half-cone angle of the tip, and R is the radius of the tip apex. Fig 5.2 shows the comparison of the electrostatic force on cantilever body only and the total

40

electrostatic force, computed for the fundamental and second resonant modes and for the KPM system constructed in this work. It is seen that the contribution of the body to the total electrostatic force is suppressed in the second resonant mode by more than an order of magnitude. For a specific tip sample separation depending on the cantilever geometry, the body interaction can be eliminated altogether.
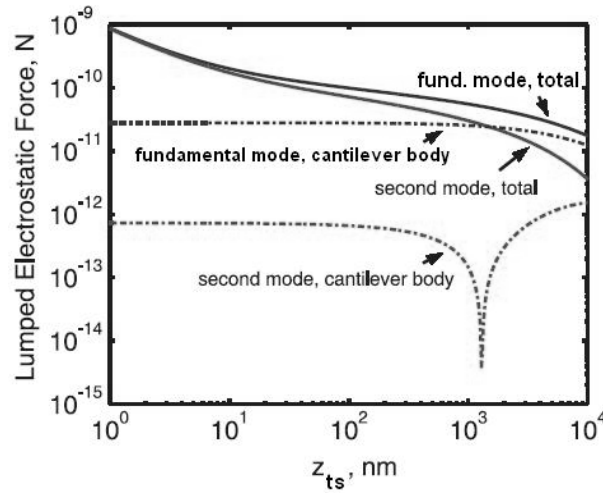
Figure 5.2. Comparison of lumped electrostatic forces on the cantilever for the fundamental and second resonant mode, calculated using the parameters of the cantilever used in the work.

In multimode KPM imaging, the fundamental mode is used in the topography feedback loop and is driven by a piezoelectric or capacitive actuator mounted on the probe holder. The second mode is used in the KPM loop and is driven by an ac bias applied on the probe or the sample. The actuation for the second order mode is thus much weaker than that of the fundamental mode due to the small area of the probe over the sample. As a result, in normal operation the amplitude of oscillation for the second mode is much smaller compared to that of the fundamental mode. In this case, the equations of motion for the two modes can be separated. The deflection amplitudes for the higher order modes can be calculated from the ac force using

$$A_n = Q_n \frac{F_{AC,n}}{k_n} \tag{5.5}$$

Where k_n is the lumped spring constant and $F_{AC,n}$ is the ac lumped force and Q_n is the quality factor associated with the resonant mode. In calculating the electrostatic force, the effect of oscillation in the fundamental mode must be taken into account. Oscillation amplitude A_1 of fundamental mode is fixed by the topography feedback loop. Tip sample separation then becomes $z_{ts} = A_1 + A_1\cos(\omega_1 t)$ neglecting the second mode oscillation. Variation in tip sample separation modifies the electrostatic force. In the electrostatic force in the second resonant mode thus needs to be averaged over many periods of the fundamental mode to filter out the effect of the fundamental mode. For the multimode KPM system built in this thesis work, the electrostatic force in the second order mode is calculated to be typically 2×10^{-11} N. Quality factor for the second mode was measured to be 450. The lumped spring constant for higher modes can be calculated from the one for the fundamental mode ($k_1 = 2.8$ N/m for the probe used) using power balance arguments as

$$k_n = k_1 \omega_n^2 / \omega_1^2 \tag{5.6}$$

resulting in a second mode spring constant of $k_2 = 120$ N/m for the probe used. Using these, the oscillation amplitude for the second mode was calculated to be 0.1 nm, in reasonable agreement with the experimental observations.

5.3 Multimode KPM Operation

The KPM system built over the PSIA XE100E AFM system is modified to be used in multimode KPM imaging under supervision of Dr. Aykutlu Dâna. Working in air, the commercial AFM system has necessary auxiliary connections to enable it to be expanded for other applications. Using an auxiliary ADC signal input and a signal output for the probe read-out signal, a Stanford Research Systems (SRS) SR844 analog RF lock-in amplifier [37], a SRS DS345 synthesized function generator [31],

and a SRS SIM960 programmable analog PID controller [32] are added to the system. A block diagram for the expanded system is shown in Figure 5.3. Cantilever oscillation signal containing both fundamental and second resonant modes is fed into the RF lock-in which is locked to the function generator set to the second mode frequency. The amplitude of the downconverted signal is inputted to the PID controller, with its parameters are set in order to null the input signal. The near dc output is connected to an auxiliary ADC input of the AFM control unit which is to be displayed and saved as an image. The same signal is added to the signal generator output and the sum signal is applied as a bias to the probe with the sample being grounded. As discussed before in chapter 4, first harmonic of the electrostatic force is proportional to $V_{cpd} - V_{DC}$, thus when it is nulled the dc bias equates the contact potential difference.
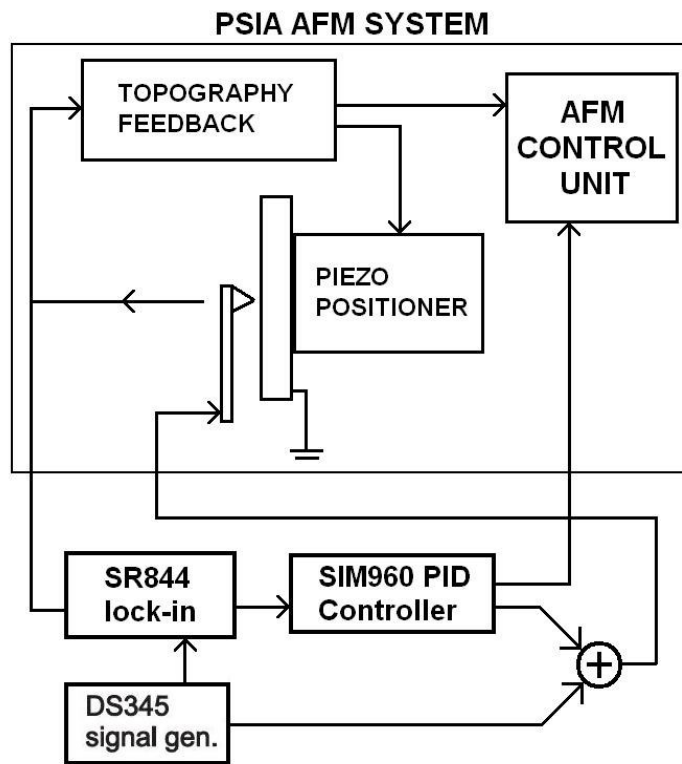

Figure 5.3. Configuration of the multimode KPM system built on a PSIA XE100E AFM.

Pt/Ir tips that was used with the system was coated by 10 nm thick silicon nitride in a PECVD reactor at Bilkent University Advanced Research Laboratory by Dr. Aykutlu Dâna. The cantilever has a rectangular cross section with a length of 220 μm and width of 30μm. The tip height is 15μm, the half-cone angle is 30° and the tip radius is 20 nm. The first and second resonant modes were measured to be at 70.01 kHz and 448.83 kHz. The quality factors corresponding to these frequencies were measured to be around 220 and 450 respectively suggesting less air damping of the second resonant mode because of the mode shape has a node along the length of the cantilever dictating a less average displacement.

5.4 Electrostatic Spectroscopy

When the probe is in electrostatic interaction with the sample, the variation in the force can be measured with respect to varying dc bias voltage to examine the nature of the interaction and to reveal charging and discharging effects [38]. There are cases when the ability to perform latter type of measurements relies on the use of relatively high dc bias voltages. Application of high bias voltages may lead to modifications in both the tip and the sample. Coating the tip with a layer of insulator thin enough to allow a tunneling current can be a solution to the problem. Use of the insulating layer will lead to increased tip sample separation, which can be partially avoided by the use of higher order resonant modes with lower oscillation amplitudes.

Samples characterized in this work are typically semiconductor nanocrystals or other nanoparticles that are located on a bulk semiconductor substrate surface or embedded into an insulating layer which itself is coated on bulk semiconductor substrate. Electrostatic interaction energy stored in the field between the tip and sample, when there is a nanocrystal in between them with a charge q can be calculated as

$$U = \frac{q^2}{2C_t} - \frac{C_1}{2C_t}qV - \frac{C_1 C_2}{2C_t}V^2 - \frac{C_0}{2}V^2 \qquad (5.7)$$

44

where C is the capacitance of the tip and the sample, C_1 is the capacitance between tip and the nanocrystal, C_2 is the capacitance between the nanocrystal and the substrate and C_t is the total capacitance seen by the tip. From (5.7), the electrostatic force acting on the tip can be calculated by differentiating with respect to the tip sample seperation z, as

$$F_e = \frac{1}{C_t} \frac{\partial C_1}{\partial z} \left(\frac{q^2}{2} - C_2 qV + \frac{C_2^2 V^2}{2} \right) + \frac{1}{2} \frac{\partial C_0}{\partial z} V^2 \tag{5.8}$$

If a charge q is deposited in the nanocrystal between the force-voltage measurements, then there will be a shift between the corresponding curves. The voltage shift can be calculated as

$$\Delta V_H = \frac{q}{C_2} \left(1 + \frac{\partial C_0}{\partial z} \bigg/ \left(\frac{C_2}{C_1 + C_2} \right)^2 \frac{\partial C_1}{\partial z} \right)^{-1} \tag{5.9}$$

The configuration used for multimode KPM imaging is modified for making spectroscopy measurements. An auxiliary DAC output on SR844 lock-in amplifier is used for supplying the dc bias to the probe. This voltage is added to the function generator output to form the dc + ac probe drive signal. A Delphi program is written to control the voltage sweep and processing the data.

5.5 Multimode KPM Application

5.5.1 Gold and Silver Nanoparticles

First samples to be studied were gold and silver nanoparticles on silicon surface with average diameters of 10 nm and 20 nm respectively. The nanoparticles were deposited by drop casting an emulsion with water base, and subsequent room temperature evaporation. The nanoparticles were kindly supplied by Prof. Dr. Şefik Süzer. Kelvin Probe data is taken by incorporating the potential nulling loop using

the second resonant mode. Figure 5.4 shows an image taken from a sample with both Au and Ag particles. Topography, contact potential difference and phase of the fundamental mode signal are shown on a, b, and c respectively. The final image d, combines three of the former with their respective colors.
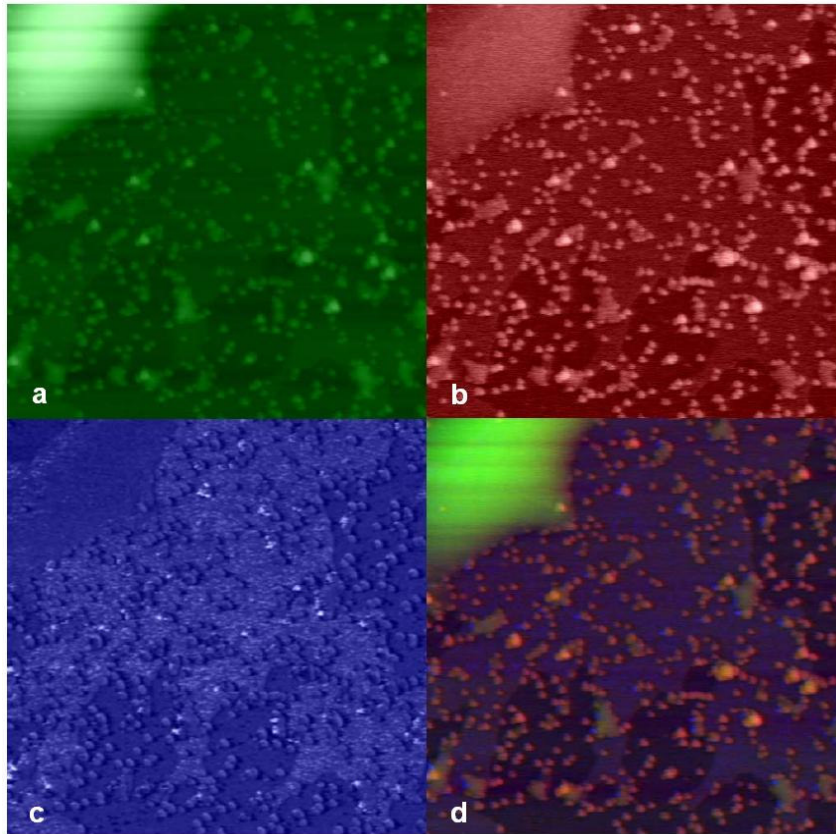

Figure 5.4. Au and Ag nanoparticles on silicon. a) topography, b) contact potential difference, c) phase of the fundamental mode, and d) combined image.

The high feature on the top left corner of the topography image is believed to be an organic contamination height of which is measured to be 70 nm from the topography data. Au and Ag nanoparticles appear as the smaller peaks scattered to the image area. It can be seen from the contact potential difference image that the contrast of the nanoparticles are greater than that of the contamination particle which however is much taller. Reason for the low contrast is possibly the low electrical conductance of the contamination.

Electrostatic spectroscopy data is gathered from another sample coated with only silver nanoparticles again with 10nm average diameters. Figure 5.5 shows the signal amplitude variations in dc bias voltage sweep from +2V to -2V and then back to +2V. The data is taken with the probe tip at distance from the sample so that the main contribution to the electrostatic force comes from the cantilever body. In Fig. 5.5a the driving ac bias is at fundamental mode frequency, while in Fig 5.5b it is at second mode frequency. It is seen that the cantilever body interaction is much weaker when using the second resonant mode.
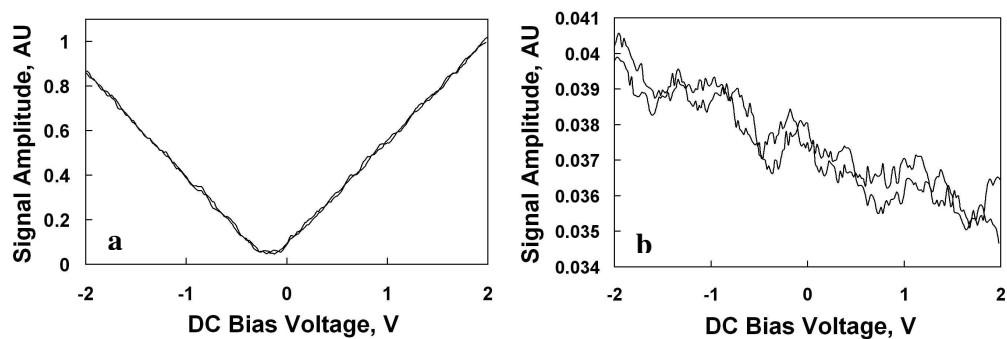

Figure 5.5. Probe signal on dc bias voltage sweep with ac driving signal is at a) fundamental mode frequency and b) second mode frequency.

Figure 5.6 shows another dc bias voltage sweep from +1.5V to -1.5V and back to +1.5V, using the second resonant mode, with probe in contact with the sample. Fig. 5.6a is the signal amplitude and Fig. 5.6b is the signal phase. Signal amplitude decreases up to a value (-0.45V) of dc voltage and starts to increase. The amplitude is not completely nulled due to the effects of stray capacitances between the probe and the driving piezo actuator. Signal phase changes rapidly around -0.45V due to the sign change in $V_{cpd} - V_{DC}$ and further indicates that there is electrostatic interaction. The plots have little or no hysteresis. This suggests that the sample is not charged during the sweep.
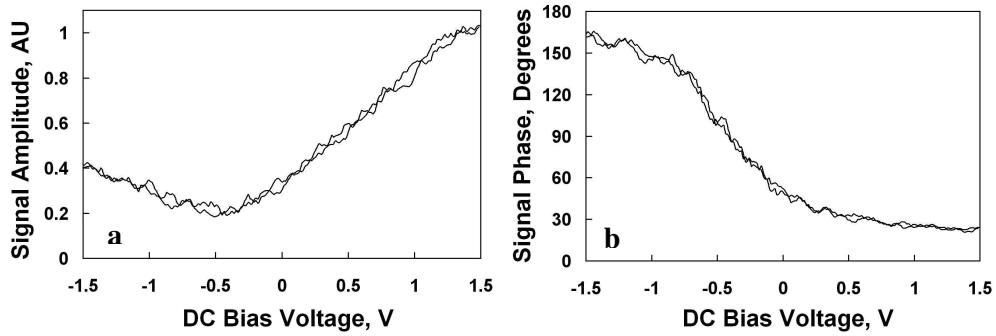
Figure 5.6. Dc voltage bias sweep with second mode ac drive signal. a) probe signal amplitude and b) phase.

5.5.2 Germanium Nanocrystals on Silicon Surface

This sample was prepared by sputter coating a 5nm layer of germanium on cleaned silicon surface and subsequent 45 minute annealing with non-uniform temperature profile in high vacuum. The substrate was a p-type doped (100) silicon wafer. A KPM image taken from the sample is shown on figure 5.7. Germanium nanocrystals show contrast with the silicon surface.
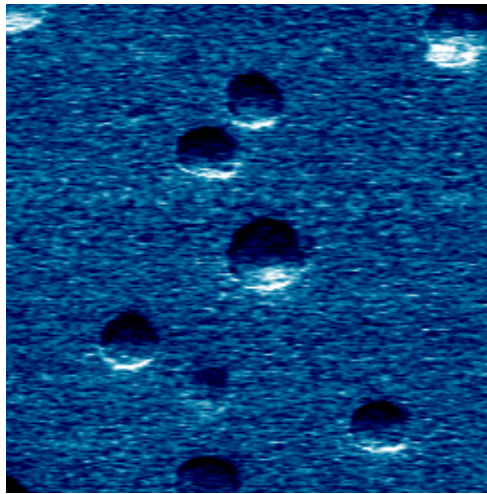

Figure 5.7. KPM image of germanium nanocrystals on silicon substrate.

Figure 5.8 shows a dc bias voltage sweep from +1V to -1V and back to +1V using the second mode frequency for the ac driving signal. The probe is in contact with a

nanocrystal, and the plot shows electrostatic interaction indicating a contact potential difference. Lack of hysteresis indicates that the nanocrystal charging is insignificant for this voltage sweep.
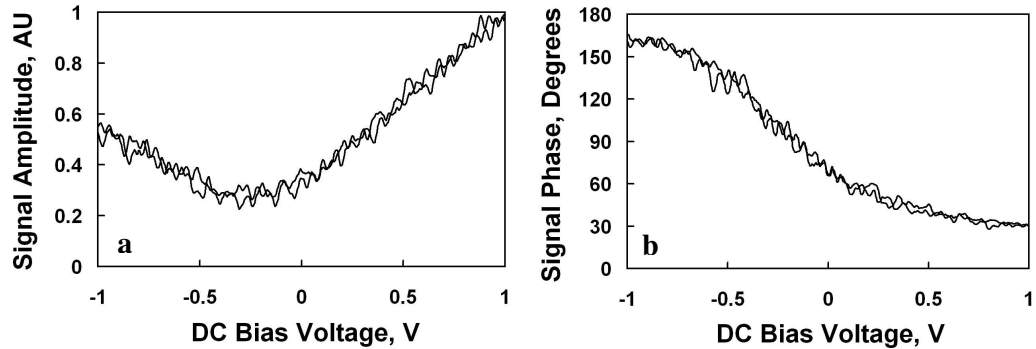
Figure 5.8. Dc voltage bias sweep with second mode ac drive signal. a) probe signal amplitude and b) phase.

Figure 5.9 shows a dc bias voltage sweep from +3V to -3V and back to +3V using the second mode frequency for the ac driving signal. The probe is in contact with the same nanocrystal as in figure 5.8. Plots having hysteresis indicates that there is a shift in electrostatic potential in the sample. A possible explanation is the charging of the nanocrystal in touch, changing its potential. Because the nanocrystal resides on the surface of p-type doped silicon, the charge should be consisting of holes confined in the barrier formed by the germanium silicon interface.
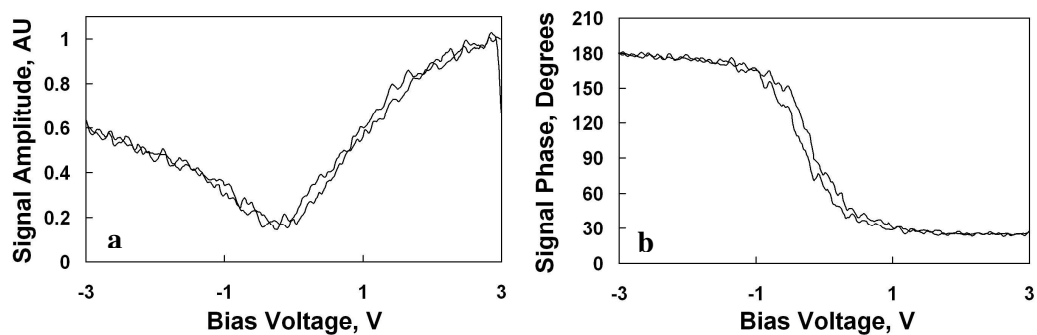
Figure 5.9. dc voltage bias sweep with second mode ac drive signal. a) probe signal amplitude and b) phase.

More pronounced hysteresis is observed using another sample, which contained silicon nanocrystals embedded in silicon nitride produced by Dr. Dâna. The nanocrystals were formed by coating a silicon substrate with silicon nitride and excess silicon using PECVD and subsequent annealing. Figure 5.10 shows the result of a bias voltage sweep from +2V to -2V and back to +2V. The increase in shift complies with the possible increase in charge holding capacity due to the nanocrystals being embedded in an insulating matrix.
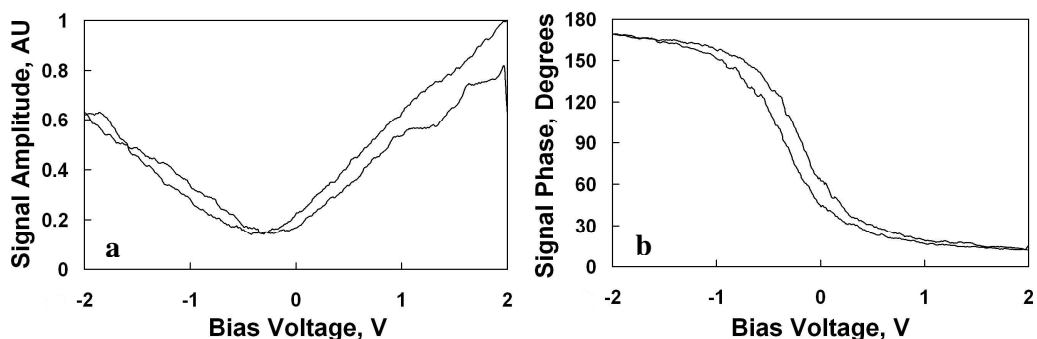

Figure 5.10. dc voltage bias sweep with second mode ac drive signal. a) probe signal amplitude and b) phase

CHAPTER 6

CONCLUSION AND FURTHER WORK

An atomic force microscope is developed and implemented. The prototype system successfully imaged nanometer scale structures using piezoresistive cantilever probes. The system worked with good stability in the z direction.

Germanium nanocrystals formed over silicon surface using sputter coating and subsequent annealing show variation in size for varying conditions. The samples are grown with the aim of observing quantum dot charging effects; as a result fabrication of more samples with small size isolated nanocrystals was intended. The first method applied was using the same annealing temperature, while varying the amount of coated germanium. Reduction in nanocrystal size is observed with thinner initial coatings. However, the nanocrystals are adjacent to each other. The second method was to anneal the sample in a varying temperature profile. Reduction in nanocrystal size in cooler regions are observed.

Multimode Kelvin Probe imaging is implemented using a commercial AFM system. Electrostatic interaction of the cantilever body with the sample is measured for the first and second order resonant modes and significant reduction in body interaction for the second order resonant mode is observed. Kelvin probe operation at room temperature in air is achieved. Reduction in tip swing in second order resonant mode due to the mode shape improved the average tip sample separation. This allows the use of a thin insulator layer coated on the tip while maintaining adequate electrostatic

interaction of the tip with the sample. With the insulating layer, tip to sample biases of up to 5 Volts are successfully applied. Charging in isolated nanocrystals both on semiconductor surface and embedded into insulating matrix are observed.

A laser interferometer detection system will be integrated with the AFM. This will enable operation with commercially available cantilevers. The detection noise is expected to decrease. Also, using conducting probes, application of bias voltages to the probe tip will be possible and this will enable operation in Kelvin probe mode. The system will be able to operate using the developed multimode Kelvin probe microscopy method. The system will be next placed in the vacuum chamber. Operation in high vacuum condition will improve the quality factor of the cantilever, which will improve noise performance. In-situ characterization of samples fabricated using sputter coating and subsequent annealing will be possible.

REFERENCES

[1] G. Binnig, H. Rohrer, "Scanning tunneling microscopy–from birth to adolescence", *Reviews of Modern Physics*, vol. 59, pp. 615-625, 1987.

[2] G. Binnig, H. Rohrer, "In touch with atoms", *Reviews of Modern Physics*, vol. 71, pp. S324-S330, 1999.

[3] F. J. Giessibl, "Advances in atomic force microscopy", *Reviews of Modern Physics,* vol.75, pp.949-983, 2003.

[4] G. Binnig, C. F. Quate, Ch. Gerber, "Atomic Force Microscope", *Physical Review Letters*, vol. 56, pp. 930-933, 1986.

[5] Nanoworld Innovative Technologies, http://www.nanoworld.com, Last accessed August 2007.

[6] M. L. Bloo, H. Haitjema, W. O. Pril, *Measurement*, **25**, pp. 203-211, 1999.

[7] T. R. Albrecht, P. Grutter, H. K. Horne, and D. Rugar, Journal of Applied Physics, **69**, 668, (1991).

[8] U. Dürig, O. Züger, A. Stalder, Journal of Applied Physics, **72**, 1778, (1992).

[9] Newport Corporation, "MFA Series Miniature Linear Stages", http://www.newport.com/file_store/PDFs/tempPDFs/e4673_MFA-Series-Miniature-Linear-Stages.pdf, Last accessed August 2007.

[10] Newport Corporation, http://www.newport.com/file_store/PDFs/tempPDFs/e3229_ESP300.pdf, Last accessed August 2007.

[11] F. Ho, Y. Yamamoto, Journal of Vacuum Science and Technology B, **16**, 43, (1998).

[12] T. Fukuma, M. Kimura, K. Kobayashi, K. Matsushige, H. Yamada, Review of Scientific Instruments, **76**, 053704, (2005).

[13]   Fiber Optic Interferometer Fabry-Perot, http://physics-animations.com /sensors/English/interf.htm, Last accessed August 2007.

[14]   National Instruments, http://www.ni.com/pdf/products/us /20044546301101dlr.pdf, Last accessed August 2007.

[15]   L. F. Johnson, G. W. Kammlott, K. A. Ingersoll, Applied Optics, **17**, 1165, (1978).

[16]   D. Y. Kim, S. K. Tripathy, L. Li, J. Kumar, Applied Physics Letters, **66**, 1166, (1995).

[17]   G. Margaritondo, Physical Review B, **31,** 2526, (1985).

[18]   D. J. Eaglesham, M. Cerullo, Physical Review Letters, **64**, 1943, (1990).

[19]   M. Zimke-Allmang, L. C. Feldman, S. Nakahara, B. A. Davidson, Physical Review B, **39**, 7848, (1989).

[20]   Park Systems, http://parkafm.com/publications/datasheets/XE-100_Product_datasheet.pdf, Last accessed August 2007.

[21]   The Kelvin Probe Information Site, "Kelvin Probe Information", http://www.kelvinprobe.info/index.html, Last accessed August 2007.

[22]   I. D. Baikie, E. Venderbosch, J. A. Meyer, P. J. Z. Estrup, Review of Scientific Instruments, **62**, 725, (1991).

[23]   M. Nonnenmacher, M. P. O'Boyle, H. K. Wickramasinghe, Applied Physics Letters, **58**, 2921, (1991).

[24]   J. M. R. Weaver, D. W. Abraham, Journal of Vacuum Science and Technology B, **9**, 1559, (1991).

[25]   A. K. Henning, T. Hochwitz, J. Slinkman, J. Never, S. Hoffman, P. Kaszuba, C. Daghlian, Journal of Applied Physics, **77**, 1888, (1995).

[26]   R. Mackel, H. Baumgartner, J. Ren, Review of Scientific Instruments, **64**, 694, (1993).

[27]   H. O. Jacobs, P. Leuchtmann, O. J. Homan, A. Stemmer, Journal of Applied Physics, **84**, 1168, (1998).

[28]   The Generalized Multipole Technique for Computational Electromagnetics, Ch. Hafner, Artech House, 1990.

[29]   P. Girard, M. Ramonda, D. Saluel, Journal of Vacuum Science and Technology B, **20**, 1348, (2002).

[30]   Stanford   Research   Systems,   http://www.thinksrs.com/downloads/PDFs /Manuals/SR830m.pdf, Last accessed August 2007.

[31]   Stanford   Research   Systems,   http://www.thinksrs.com/downloads/PDFs /Manuals/DS345m.pdf, Last accessed August 2007.

[32]   Stanford   Research   Systems,   http://www.thinksrs.com/downloads/PDFs /Manuals/SIM960m.pdf, Last accessed August 2007.

[33]   Ch. Sommerhalter, Th. W. Matthes, Th. Glatzel, A. Jager-Waldau, M. Ch. Lux-Steiner, Applied Physics Letters, **75**, 286, (1999).

[34]   J. A. Turner, J. S. Wiehn, Nanotechnology, **12**, 322330, (2001).

[35]   E. Bonaccurso, F. Schonfeld, H. J. Butt, Physical Review B, **74**, 085413, (2006).

[36]   B. M. Law, F. Rieutord, Physical Review B, **66**, S165, (2005).

[37]   Stanford   Research   Systems,   http://www.thinksrs.com/downloads /PDFs/Manuals/SR844m.pdf, Last accessed August 2007

[38]   A. Dâna, Y. Yamamoto, Nanotechnology, **16**, S125, (2005).